Backside-illuminated scientific CMOS detector for soft X-ray resonant scattering and ptychography

Kewin Desjardins,* Kadda Medjoubi, Maurizio Sacchi, Horia Popescu, Roland Gaudemer, Rachid Belkhou, Stefan Stanescu, Sufal Swaraj, Adrien Besson, Jaianth Vijayakumar, Stéphanie Pautard, Arafat Noureddine, Pascal Mercère, Paulo Da Silva, Fabienne Orsini, Claude Menneglier and Nicolas Jaouen

Synchrotron SOLEIL, Saint-Aubin, Gif-sur-Yvette, 91192, France.
*Correspondence e-mail: kewin.desjardins@synchrotron-soleil.fr

The impressive progress in the performance of synchrotron radiation sources is nowadays driven by the so-called 'ultimate storage ring' projects which promise an unprecedented improvement in brightness. Progress on the detector side has not always been at the same pace, especially as far as soft X-ray 2D detectors are concerned. While the most commonly used detectors are still based on microchannel plates or CCD technology, recent developments of CMOS (complementary metal oxide semiconductor)-type detectors will play an ever more important role as 2D detectors in the soft X-ray range. This paper describes the capabilities and performance of a camera equipped with a newly commercialized backside-illuminated scientific CMOS (sCMOS-BSI) sensor, integrated in a vacuum environment, for soft X-ray experiments at synchrotron sources. The 4 Mpixel sensor reaches a frame rate of up to 48 frames s^{-1} while matching the requirements for X-ray experiments in terms of high-intensity linearity (>98%), good spatial homogeneity (<1%), high charge capacity (up to 80 ke^{-}), and low readout noise (down to 2 e^{-} r.m.s.) and dark current (3 e^{-} per second per pixel). Performance evaluations in the soft X-ray range have been carried out at the METROLOGIE beamline of the SOLEIL synchrotron. The quantum efficiency, spatial resolution (24 line-pairs mm^{-1}), energy resolution (<100 eV) and radiation damage versus the X-ray dose (<600 Gy) have been measured in the energy range from 40 to 2000 eV. In order to illustrate the capabilities of this new sCMOS-BSI sensor, several experiments have been performed at the SEXTANTS and HERMES soft X-ray beamlines of the SOLEIL synchrotron: acquisition of a coherent diffraction pattern from a pinhole at 186 eV, a scattering experiment from a nanostructured Co/Cu multilayer at 767 eV and ptychographic imaging in transmission at 706 eV.

1. Introduction

Third-generation synchrotron sources provided X-ray beams of much improved flux and transverse coherence and have allowed the development of a large range of new X-ray experiments. Nowadays, many direct 2D detectors are commercially available for hard X-ray applications (Förster *et al.*, 2019) with demonstrated high frame rates, charge capacity, efficiency and spatial resolution. However, a wide gap exists in the soft to tender X-ray domain (10 eV to 3 keV) where the experiments are not able to fully benefit from the performance offered by modern facilities. The detectors used at soft X-ray end-stations are typically based on backside-illuminated CCD (CCD-BSI) sensors such as the commercial cameras from Princeton PI-MTE (https://www.princetoninstruments.com), GreatEye GE-VAC (https://www.greateyes.de) or others equipped with cooled CCD-BSIs. This kind of detector is compact enough, vacuum compatible [10^{-9} mbar (1 mbar =

Irradiation X-ray spots
1600 eV
560 eV
160 eV
1000 eV
Dose level
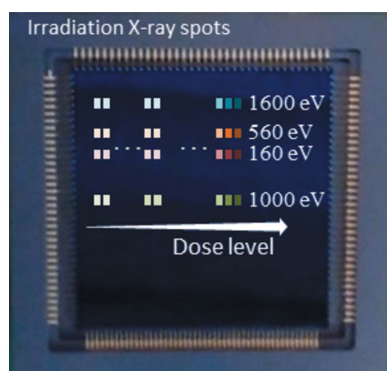
100 Pa)], and offers good performance as demonstrated at many synchrotron beamlines (Chauleau *et al.*, 2018), but also at laser-based X-ray sources (Lambert *et al.*, 2015) and at X-ray free-electron laser (XFEL) facilities (Pedersoli *et al.*, 2011). However, the available commercial CCD sensors suffer from the severe limitation of their readout speed. Indeed, in order to limit the readout noise and guarantee a high signal-to-noise ratio allowing single X-ray photon sensitivity, the frame rate has to be reduced to less than 1 frame s^{-1}. As an example, X-ray Fourier transform holography (FTH) experiments at the COMET end-station (Popescu *et al.*, 2019) of the SEXTANTS beamline (Sacchi *et al.*, 2013), the soft X-ray scattering beamline of the SOLEIL synchrotron, are performed with a dead-time of 97.5% due to the readout time in full-chip mode (typically 0.1 s of X-ray collection is followed by 4 s of readout).

In order to fulfil the fast readout requirement combined with high sensitivity, several new advanced detector systems are under development or have been recently developed, and some have been implemented in soft X-ray experiments in synchrotron sources, *e.g.* (i) Fast-CCD (Denes *et al.*, 2009) featuring low readout noise with a high frame rate (60 frames s^{-1} for 960 × 1920 pixels) by increasing the number of readout ports; (ii) hybrid pixel detectors (Jungmann-Smith *et al.*, 2016; Bergamaschi *et al.*, 2018) based on a low-noise, high-dynamic and high-frame-rate charge integration readout system; (iii) pnCCD, a fast and low-noise 2D spectroscopic detector (Strüder, 2016); (iv) CMOS (complementary metal oxide semiconductor)-based sensors such as silicon-on-insulator (SOI) technology (Arai *et al.*, 2010), DEPFET sensors (Porro *et al.*, 2012) for very high frame rate soft XFEL applications, the PERCIVAL detector (Wunderer *et al.*, 2014), again under development by a consortium of synchrotrons, or recently the Pippers MAPS (monolithic active pixel sensor) technologies (El Bitar *et al.*, 2019).

Recently, a new generation of large backside-illuminated scientific CMOS sensors (sCMOS-BSI) has been developed (Ma *et al.*, 2015) and commercialized by GPIXEL (https://www.gpixel.com/). It was especially designed in order to optimize the efficiency in the visible-light range (>95% at 550 nm) and to retain the good performance of the first generation of sCMOS sensors (low readout noise, large full well capacity and high frame rate). This new cost-efficient and competitive 4 Mpixel sensor has been demonstrated to be well suited for soft X-rays, and has already been characterized for several applications such as soft X-ray resonant scattering (Desjardins *et al.*, 2019) or X-ray imaging spectroscopy (Wang *et al.*, 2019). In this paper, we describe the integration of this sCMOS-BSI into an in-house-developed vacuum-compatible camera and its characterization. The performance has been evaluated at the METROLOGIE beamline (Idir *et al.*, 2006) and is reported in the following sections. In particular, we have characterized the sCMOS-BSI camera dynamics (including dark current, readout noise, spatial uniformity, linearity and overall gain), the soft X-ray quantum efficiency in the energy range between 40 and 2000 eV, as well as the spatial and energy resolution, and the radiation tolerance. We also report on different proof-of-principle experiments using this sCMOS-BSI camera: acquisition of a coherent diffraction pattern from a 5 μm pinhole at 186 eV at the METROLOGIE beamline, a soft X-ray resonant scattering experiment from a nanostructured Co/Cu multilayer at 767 eV on the SEXTANTS beamline (Sacchi *et al.*, 2013) and several soft X-ray ptychography reconstructions at 706 eV on the HERMES beamline (Belkhou *et al.*, 2015).

2. Soft X-ray camera description

2.1. sCMOS GSENSE400BSI characteristics

The integrated and characterized sensor is the scientific CMOS backside-illuminated GPIXEL GSENSE400BSI [Fig. 1(*a*)], a 4 Mpixel (2048 × 2048 resolution, 11 μm × 11 μm pixel size) high-dynamic-range sensor based on standard 4T pixel architecture (Ma *et al.*, 2015) with two electronic gains [high gain (HG), low gain (LG)] and a combined gain mode in order to achieve the so-called HDR (high dynamic range) mode. Firstly integrated by TUCSEN (http://www.tucsen.com) on the Dhyana95 camera, this sensor is now widely integrated as in the PHOTOMETRICS Prime95 (https://www.photometrics.com/), the ANDOR Sona (https://andor.oxinst.com/) or others. These cameras take advantage of the characteristics of the sensor in terms of the readout noise (<2 e$^-$ r.m.s.), the relatively large full well capacity (FWC; up to 80 ke$^-$), good performance in terms of spatial noise [dark signal non-uniformity (DSNU) < 5 e$^-$ and photo response non-uniformity (PRNU) < 1%] and respectable results in terms of dark current (∼3 e$^-$ per second per pixel with sensor cooled at −20°C). The full-frame GSENSE400BSI sensor acquisition speed can reach 48 Hz for standard gain mode (LG or HG) and is limited to 24 Hz for the HDR mode. This performance, summarized in Table 1, has been measured using visible light with the Dhyana95 camera (Desjardins *et al.*, 2019; Wang *et al.*, 2017) following the EMVA1288 standard (https://www.emva.org).

Following these specifications, the signal-to-noise ratio (SNR) of the GSENSE400BSI, defined by equation (1), has been calculated for the different modes and compared with
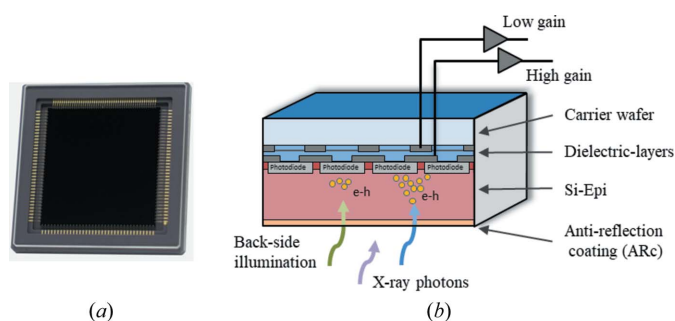

Figure 1
sCMOS GSENSE400BSI sensor. (*a*) Sensor picture (GPIXEL, https://gpixel.com) and (*b*) schematic cross section of the sensor (Wang *et al.*, 2019).

Table 1
Electro-optical characteristics of the GSENSE400BSI sensor specifications and TUCSEN Dhyana95 camera measurements results.

	Symbol	Value	References
Gain	K	LG, HG or HDR mode	
Frame rate	frames s^{-1}	24 Hz full frame (HDR), 48 Hz full frame (LG or HG)	
Readout architecture		Rolling shutter	GPIXEL datasheet (https://www.gpixel.com/)
Pixel size	pixel	11 µm × 11 µm	TUCSEN Dhyana95 datasheet (http://www.tucsen.com/
Sensor size		4 Mpixel, 2048 × 2048 pixels (22.5 mm × 22.5 mm)	en.html)
Exposure time	t	20 µs–10 s	
Binning		No	
Readout noise	σ_{read}	<2 e$^-$ r.m.s. (HDR and HG) and <45 e$^-$ r.m.s. (LG)	
Dark current	μ_{dark}	~3 e$^-$ s^{-1} pixel^{-1} (−20°C)	Desjardins *et al.* (2019), Wang *et al.* (2017)
Full well capacity	FWC	30 ke$^-$ (HDR), 1700 e$^-$ (HG) and >80 ke$^-$ (LG)	
Spatial pixel offset noise	DSNU	<5 e$^-$	
Spatial pixel gain noise	PRNU	<1%	

Table 2
Electro-optical characteristics of the GSENSE400BSI sensor, PIMTE CCD-BSI and PERCIVAL detector used in SNR estimation.

	PI-MTE CCDBSI (datasheet PIMTE-2048B)	PERCIVAL (BSI) (Khromova *et al.*, 2016)	GSENSE400BSI (Desjardins *et al.*, 2019; datasheet Dhyana95)
Pixel size	13.5 µm × 13.5 µm	27 µm × 27 µm	11 µm × 11 µm
QE (500 eV)	0.85	Unpublished	0.5 up to 0.8 (see Section 3.2)
Readout noise	10 e$^-$ r.m.s. (1 MHz ADC)	15 e$^-$ r.m.s. (HG), 1600 e$^-$ r.m.s. (LG)	2 e$^-$ r.m.s. (HG or HDR), 38 e$^-$ r.m.s. (LG)
Dark current	0.02 e$^-$ s^{-1} pixel^{-1} (−50°C)	Unpublished	3 e$^-$ s^{-1} pixel^{-1} (−20°C)
FWC	100 ke$^-$	~4 Me$^-$ pixel^{-1} (LG), ~2000 e$^-$ (HG)	80 ke$^-$ (LG), 30 ke$^-$ (HDR), 1600 e$^-$ (HG)

values obtained for other similar sensors in the soft X-ray domain (Fig. 2):

$$\text{SNR} = S/\Big[\underbrace{\sigma_{\text{read}}^2 + \mu_{\text{dark}} \times t}_{\text{temporal noise}} + \underbrace{S \times \left(F + \text{QE} \times \tfrac{E}{3.65}\right)}_{\text{shot noise and Fano noise}}$$
$$+ \underbrace{\text{DSNU}^2 + \text{PRNU}^2 \times S^2}_{\text{spatial noise}}\Big]^{1/2}. \tag{1}$$

S is the signal in (e$^-$) equal to $\text{QE} \times N \times E/3.65$ with QE the quantum efficiency depending on the beam energy E, N the number of photons, 3.65 eV the electron–hole pair creation energy in silicon, F the Fano factor (~0.12 for silicon), t the

exposure time (in s), σ_{read}, μ_{dark}, DSNU and PRNU as given in Table 1. The shot noise and Fano noise development are derived from equation (8) of Spear (2005).

Fig. 2 shows an example of the SNR for an X-ray beam of 500 eV and its comparison with published results for other sensors, *i.e.* a back-illuminated CCD (PIMTE2048B camera from https://www.princetoninstruments.com) and the PERCIVAL detector (Khromova *et al.*, 2016). In the SNR estimations only the shot noise, temporal noise (thermal noise and readout noise) and the theoretical QE (see also Section 3.2) of each sensor are taken into account while the spatial noise is excluded (PRNU = 0% and DSNU = 0 e$^-$). In this figure, we also represent the detector saturation (at 500 eV) corresponding to the FWC in photons pixel^{-1} (see Table 2 for all details).

Two versions of the sCMOS GSENSE400BSI have been evaluated: the GSENSE400BSI-TVISB, the standard visible-light-dedicated sensor version, and the GSENSE400BSI-GP, an experimental version dedicated to the UV range (Harada *et al.*, 2019), recently developed and not yet commercially available. The backside of the first, as represented on the sensor physical structure in Fig. 1(*b*), is composed of a 10 µm-thick silicon epitaxial layer (Epi-Si), 7 nm-thick SiO$_2$ followed by 63 nm-thick Si$_3$N$_4$. These topmost layers serve as an anti-reflection coating (ARc) and passivation layer (coating originally processed for visible applications). The second sensor tested was without the anti-reflective coating (no-ARc) on the photo-sensitive area and has a thinner Epi-Si layer of about 4 µm. The main interest in the GP version is the possibility of achieving greater efficiency in the so-called water windows (250 to 550 eV) as at this energy the attenuation of X-ray photons by the ARc layers (see Section 3.2) is non-negligible.
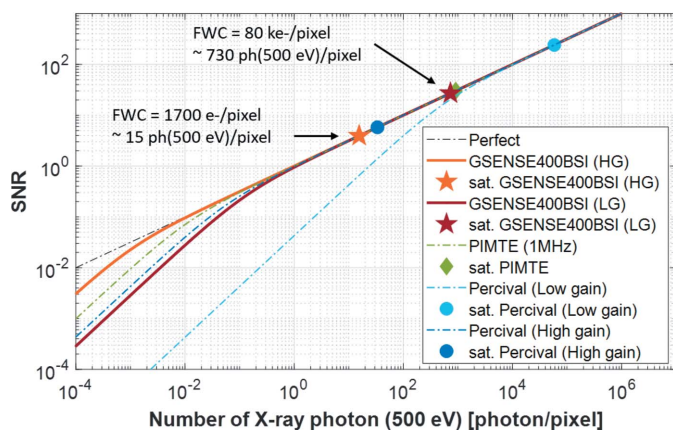

Figure 2
Example of SNR estimation for sCMOS-BSI GSENSE400BSI (low gain and high gain), PIMTE CCD-BSI (with ADC speed of 1 MHz), PERCIVAL (low gain and high gain) at 500 eV. The SNR of a perfect detector is calculated for QE = 1, noise = 0 e$^-$. The SNR of each detector is calculated from the details reported in Table 2 and considering dark noise given for 1 s of integration time. The saturation level of each sensor is shown by dots, a pentagon and stars, respectively, for PERCIVAL, PIMTECCDBSI and GSENSE400BSI.

research papers

2.2. X-ray camera design and software integration

In order to evaluate and integrate the sCMOS GENSE400BSI sensors on the soft X-ray beamlines of the SOLEIL synchrotron, a new dedicated and vacuum-compatible (10^{-6} mbar) mechanical support and housing for the TUCSEN Dhyana95 camera have been designed and fabricated (Fig. 3). However, it should be noted that the vacuum compatibility of various individual components such as the cables, Peltier module and printed circuit board (PCB) has not been the subject of in-depth study for this first prototype assembly. It is indeed a crucial technical point which will be taken into account in the development of the future detector that will be permanently installed at the SOLEIL beamlines. Indeed, as seen during our series of tests, the cooled sensor could be contaminated by, among others, dust, grease and water, which might degrade its efficiency (Deiries et al., 2016). All components that are located in vacuum, i.e. sensor, sensor board, data acquisition (DAQ) board [field-programmable gate array (FPGA), power supply, data transfer etc.], are under a water-cooling circuit (>12°C) that has been designed to maintain an optimal temperature of both the sensor (−20°C with two stages of Peltier cooler) and the electronic components. As is typically done for such soft X-ray experiments, the assembly has been designed to block parasitic light with the possibility to add different visible filters (such as thin carbon or alumina filters from Luxel, https://luxel.com) in front of the sensor. The final design remains compact enough (10 × 11 × 12 cm) to fit within the vacuum chambers on the beamlines employed in this study and the restrictions of their respective environments. Furthermore, an optional X-ray beamstop can be added in front of the camera and positioned with two linear piezo motors as shown in Fig. 3.

To transfer and record the images, this camera is connected via a USB3 interface through a dedicated UHV USB3 feedthrough to a standard Windows 64 bit computer. This computer is equipped with a Tango LIMA device (https://lima1.readthedocs.io/en/latest/) developed at SOLEIL and based on TUCAM API from TUCSEN. This allows the detector to be used with the standard control system of SOLEIL's beamlines.

The SOLEIL-redesigned camera has the same characteristics and performance as the original in terms of SNR, readout speed (24 Hz full frame in the three modes, USB3 limited), cooling and synchronization capabilities.
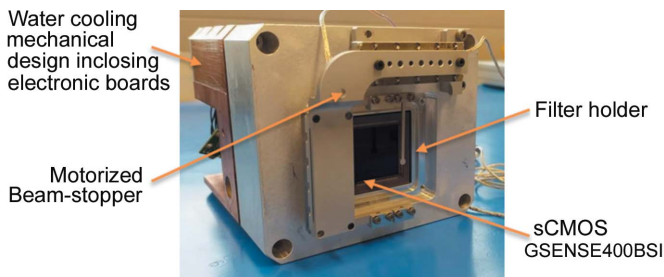

Water cooling mechanical design inclosing electronic boards

Motorized Beam-stopper

Filter holder

sCMOS GSENSE400BSI

Figure 3
Mechanical design of GSENSE400BSI camera vacuum adaptation made at SOLEIL, so-called DhyanaX.

3. Characterization test results and discussion

3.1. X-ray experimental setup

Similarly to the experimental characterization performed on the first DhyanaX prototype, presented by Desjardins et al. (2019), this X-ray camera has been mounted in the reflectometer of the soft X-ray branch of the SOLEIL METROLOGIE beamline in order to be evaluated in terms of QE (Section 3.2), spatial resolution (Section 3.3), energy resolution (Section 3.3) and sensitivity to radiation damage (Section 3.4).

All measurements have been performed with a very high spectral purity monochromatic beam, in the soft X-ray range (30–2000 eV), provided by a grating monochromator combined with the use of a series of thin filters to reduce the contamination by high-order harmonics. According to the experimental requirements, the beam size was adjusted using a set of slit apertures from 2 mm to 100 μm. The absolute incident X-ray beam flux at the entrance of the detector was measured with less than 10% of uncertainty by using a calibrated silicon photodiode (AXUV100, https://optodiode.com).

3.2. GSENSE400BSI soft X-ray efficiency

The method and measurement of the QE of the sensor have already been reported in previous work (Desjardins et al., 2019). For each step of energy (10 eV), the ratio of the number of photons detected by the sensor to the number of incident photons is calculated. The final result for both GSENSE 400BSI sensors is presented in Fig. 4 where the measurements have been superimposed with the model results proposed in equation (2):

$$QE_{model}(E) = \exp[-z_{SiO} \times \mu_{SiO}(E)] \times \exp[-z_{SiN} \times \mu_{SiN}(E)]$$
$$\times \exp[-z_{neutral} \times \mu_{Si}(E)]$$
$$\times \{1 - \exp[-z_{depleted} \times \mu_{Si}(E)]\} \quad (2)$$
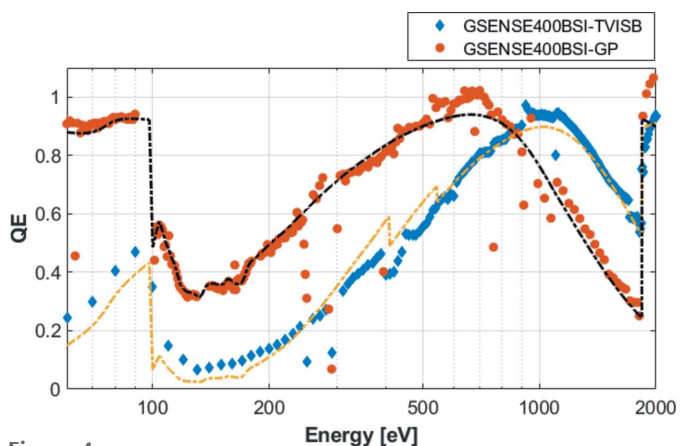

Figure 4
GSENSE400BSI-TVISB (red dots) and GSENSE400BSI-GP (blue diamonds) QE measurements compared with a theoretical model (dashed curves). The models are calculated from equation (2) with thicknesses of 30 nm of SiO_2, 63 nm of SiN_4, 11 μm for the Epi-Si and a dead layer of 60 nm for GSENSE400BSI-TVISB, and thicknesses of 4 μm Epi-Si and a dead layer of 45 nm for GSENSE400BSI-GP.

where z_{SiO} and z_{SiN} are the respective thicknesses of the two anti-reflective coatings, $z_{neutral}$ and $z_{depleted}$ are the thicknesses of the non-sensitive and sensitive silicon layers, respectively, and μ_{SiO}, μ_{SiN} and μ_{Si} are the attenuation coefficients for these different elements.

In order to fit the QE measurement results, the different parameters of the model [equation (2)] have been adjusted with a set of parameters which is a non-uniqueness solution. For the GSENSE400BSI-TVISB, the silicon oxide thickness has been increased to 30 nm, the dead layer has been adjusted to 60 nm and the Epi-Si to 11 μm. The GSENSE400BSI-GP model fitted correctly with the nominal sensor parameters consisting of a dead layer of 45 nm and an Epi-Si around 4 μm (and no-ARc layer). Both measurements and models are reported in Fig. 4.

Our results show that the QE of GSENSE400BSI is sufficient for a wide range of high-flux synchrotron applications with a maximum obtained at 1000 eV for the TVISB and 600 eV for the GP, due to the different Epi-Si thicknesses. With twice the efficiency around 300 eV, the no-ARc sensor (GP version) could be a better choice for the so-called water window region that includes the absorption K edges of C, N and O. However, it should be noted that it will be at the cost of using the thin Epi-Si layer sensor which is more sensitive to radiation damage, as will be shown in Section 3.4.

In order to illustrate its efficiency at low energies, a diffraction pattern from a 5 μm-diameter pinhole has been acquired at a beam energy of 186 eV with the sCMOS GSENSE400BSI-TVISB. The circular integration around the concentric circular rings shown in Fig. 5 demonstrated the good dynamic range of the camera which is able to visualize the first six maxima.

3.3. GSENSE400BSI spatial and energy resolution

The sCMOS GSENSE400BSI-TVISB spatial resolution has been measured using the ISO knife slanted edge method (ISO,
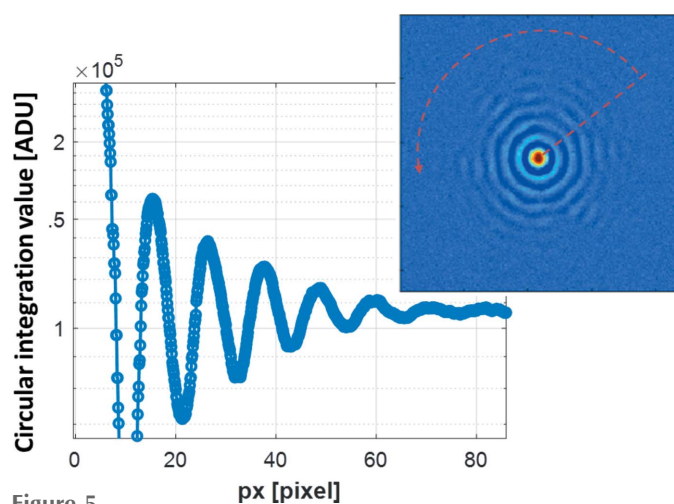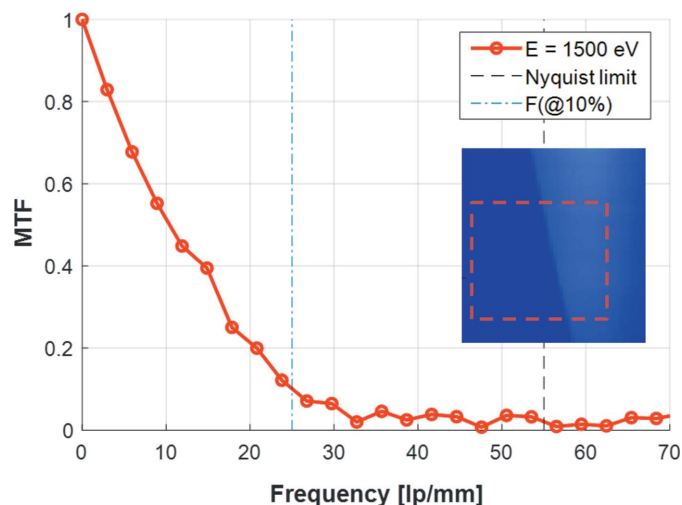

Figure 6
MTF calculation from sCMOS GSENSE400BSI-TVISB slanted edge image at 1500 eV on the METROLOGIE beamline (1000 accumulations of dark-corrected images of 100 ms).

2000). A slightly tilted silicon nitride support film has been used as the edge (the angle was about $10°$ off the pixel array alignment) illuminated with an X-ray beam at 1500 eV. The modulation transfer function (MTF) has been calculated from a cropped dark-corrected image carried out using the *sfrmat3* Matlab script (Burns, 2009). The result is given in line-pairs mm^{-1} in Fig. 6.

A 10% modulation transfer contrast is reached around 24 line-pairs mm^{-1}, corresponding to a half-pitch resolution of 21 μm, in good agreement with the sensor pixel size (11 μm^2). This resolution could be degraded for lower X-ray energies due to the lateral charge diffusion within the thick Epi-Si ($\sim$10 μm) and the neutral layer, but it was not the main object of our work. However, this effect will be discussed [Fig. 7(b)] below as it has an influence on the sensor energy resolution.

In order to characterize the energy resolution of the detector, a GSENSE400BSI-GP sensor has been exposed with a very low flux (no more than 10^6 photons s^{-1}) of monochromatic X-ray beam in order to collect images with single isolated events. For each energy, a large series of cropped images (100×2048 pixels) has been acquired with the HDR mode with a short exposure time (20 μs, $\sim$300 frames s^{-1}). This type of measurement, widely used in X-ray spectroscopy imaging and X-ray spectroscopy astronomy (Lumb *et al.*, 1984), allows the detector to be used as a counting detector with a few photons per pixel per second. For every dark-corrected image recorded, the single and isolated photon events [highlighted by blue circles in Fig. 7(a)] have been extracted and their amplitudes accumulated to obtain a spectrum. For this purpose, a Matlab script was used that isolated a pixel if its value was greater than the sum of intensities of its eight neighbouring pixels. The result is displayed in Fig. 7(b) in which we superimposed the normalized spectra for energies from 100 to 1500 eV. In order to convert the spectra to eV, the overall gain of 0.67 ADU eV^{-1} (where ADU is analog-to-digital units), calculated from this measurement, has been applied.

Figure 5
Circular integration of a pinhole diffraction image from sCMOS GSENSE400BSI-TVISB obtained at 186 eV on the METROLOGIE beamline. Top right: the 100 accumulations of 100 ms dark-corrected images in HDR mode.
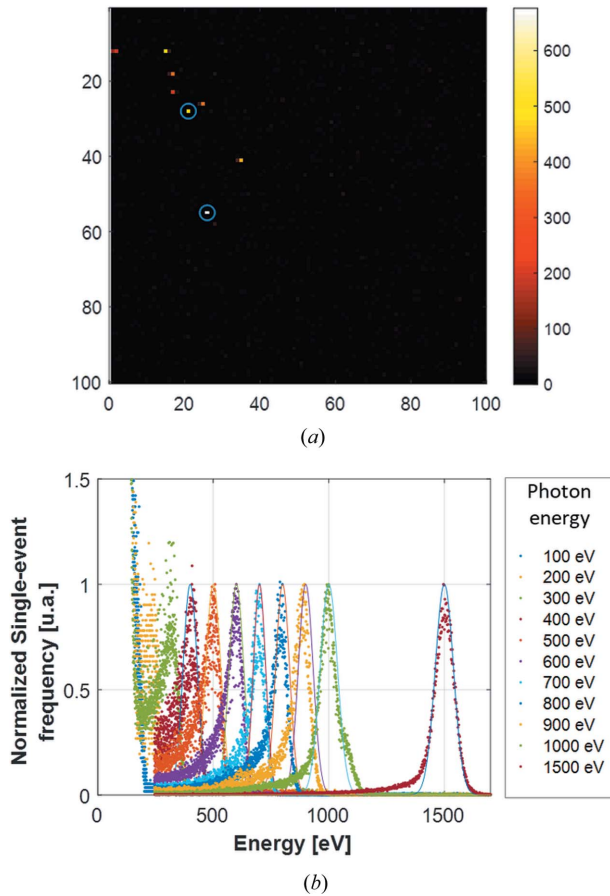
(a)

(b)

Figure 7
(a) Example of image analysed for X-ray energy beam of 1000 eV (blue circles are the pixels extracted). (b) Spectra of single-event frequencies for X-ray photon energy of 100–1500 eV. The spectra for 400–1500 eV have been manually cropped in the low-energy range (down to 200 eV).

The energy resolution is estimated by the full width at half-maximum (FWHM) of the energy peaks (Janesick, 2001) and given in Fig. 8 where the theoretical limitation given by equation (3) is also added for comparison:

$$\text{FWHM (eV)} = 2.35 \times 3.65 \times (F \times E/3.65 + \sigma_{\text{sCMOS}}^2)^{1/2}. \quad (3)$$

F is the Fano factor ($\sim$0.1 for silicon), E the photon energy, 3.65 eV is the electron–hole pair creation energy for X-ray absorption in silicon and σ_{sCMOS}^2 is the quadratic sum of noises of the sCMOS camera.

We find an energy resolution 20 eV higher than the theoretical value, due to an excess noise in this camera prototype (with readout noise > 2 e⁻ r.m.s. and higher offset and gain fixed-pattern noise). Furthermore, the sensor cooling was set to 16°C with only water cooling and the Peltier stage deactivated. The FWHM value fitted to the model with σ_{sCMOS}^2 of 6 e⁻ r.m.s. is shown in Fig. 8. Also, the noise floor, represented in Fig. 7(b) by the tail on the energy peaks, is reached for energies below 200 eV. As stated above, the effect is attributed to the charge spread created in the thick Si and particularly in the non-depleted region.
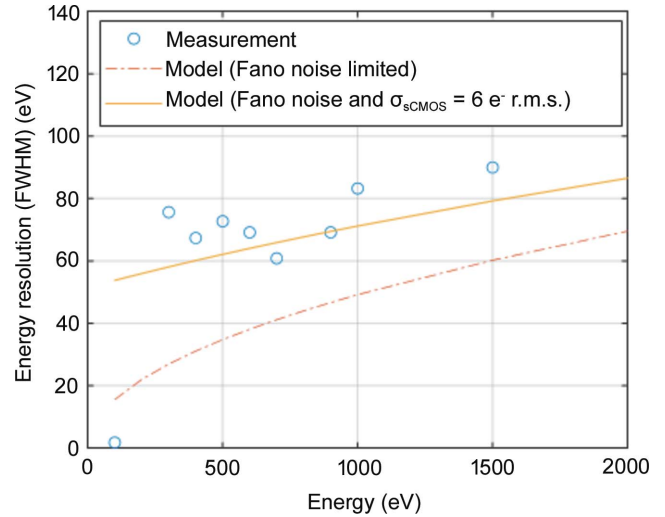

Figure 8
X-ray energy resolution of GSENSE400BSI-GP measurement results compared with the Fano noise limit and with the fitted FHWM with $\sigma_{\text{sCMOS}} = 6\,\text{e}^-$.

3.4. GSENSE400BSI radiation hardness

Considering the typical requirements for an X-ray detector needed at SOLEIL with photon energies between 40 and 2000 eV and a monochromatic flux largely exceeding 10^{12} photons s⁻¹ per 0.01% bandwidth, the radiation hardness has been evaluated on both sensors on the METROLOGIE beamline for different energies and X-ray fluxes.

The GSENSE400BSI-TVISB sensor has been locally exposed to a direct, collimated (<200 μm × 200 μm) and monochromatic X-ray beam of 160, 560, 1000 and 1600 eV and the GSENSE400BSI-GP only by a lower-energy X-ray beam of 80 eV. For each energy, the absorbed X-ray dose has been increased by increasing the time of irradiation from a few seconds to several hours [Fig. 9(a)]. We selected these characteristic energies over the wide soft X-ray energy range to evaluate the radiation damage at the different layers on the sensor's thickness: first, damage on the sensor surface considering attenuation by the anti-reflection layers; second, damage to the dielectric sensor layers, particularly the degradation on the oxide considering the AR-c and Epi-Si X-ray photon attenuation. Indeed, as shown in Fig. 10, the low-energy X-ray photons are largely absorbed in the Epi-Si while photons above 1000 eV can reach the dielectric layers due to their higher transmission. Also, the photon beam at 80 eV could penetrate the thinner Epi-Si of the GSENSE400BSI-GP (4 μm) with a transmission of about 0.1%, against below 10⁻⁵% for the GSENSE400SI-TVISB (11 μm).

The absorbed dose (D), i.e. the amount of energy absorbed per unit of mass of a given material (Ravotti, 2018), is calculated using the following equation:

$$D = \frac{\mu_{\text{en}}}{\rho}(E) \times \frac{\Phi}{A} \times t \times E \quad (4)$$

with Φ the considered X-ray photon flux, A the surface exposed by the monochromatic X-ray beam with energy E,

Table 3
Soft X-ray irradiation details for GSENSE400BSI-TVISB and GSENSE400BSI-GP.

Energy (eV)	Incident flux (Φ_0) on the sensor (total exposure time)	Absorbed dose (D) on surface (Si)	Absorbed dose (D) on dielectric layer (SiO_2)
GSENSE400BSI-TVISB			
160	4.1×10^8 photons s^{-1} (2 s to 1 h)	25 kGy to 8 MGy	Negligible [$T_{Epi-Si(10\,\mu m)} = 0$]
560	2.0×10^7 photons s^{-1} (7 s to 0.5 h)	64 Gy to 114 kGy	Negligible ($T_{Epi-Si} = 0$)
1000	1.7×10^6 photons s^{-1} (1 s to 3 h)	4 Gy to 44 kGy	0.1 Gy to 2 kGy
1600	1.2×10^7 photons s^{-1} (4 s to 5 h)	45 Gy to 180 kGy	7 Gy to 60 kGy
GSENSE400BSI-GP			
80	3.0×10^8 photons s^{-1} (0 s to 24 h)	15 kGy to 13 MGy	67 Gy to 58 kGy

μ_{en}/ρ the mass energy absorption coefficient (of Si or SiO_2) and t the exposure time.

Table 3 gives the absorbed dose (D) on both the surface and the dielectric layers of the sensor for the different energies.

As can be found elsewhere (Clarke, 1994; Hancock & Soli, 1997), one of the radiation effects on the sensor manifests in the increased pixel offset level; therefore, we have compared the dark image after irradiation with the original one for the same exposure time, as shown in Fig. 9(b). The mechanisms of these effects are complex and are not studied here but the results extracted from Fig. 9(b) are discussed. As described above, the low X-ray energy irradiation series (160 and 560 eV) with an absorbed dose up to 1 MGy(Si) into the surface layers of the GSENSE400BSI-TVISB has no effect on the pixel offset level while the high-energy X-ray irradiation series (1000 and 1600 eV) showed a significant increase in the offset level (for a lower dose) on the irradiated area [white spots on the right side of the dark image in Fig. 9(b)]. For these energies, the photons not absorbed by Epi-Si could penetrate deeply in the oxide of the electronic layers of the CMOS sensor, giving rise to relatively significant and persistent damage to the pixels (offset dark level remains high after a few weeks at room temperature). Similar effects were observed on the GSNES400BSI-GP sensor with the 80 eV beam impact.

The change in the pixel dark level ($Idark_{after\ irradiation} - Idark_0$) has been compared with the dose to the electronic layer for all irradiation series to extract an estimate of the acceptable dose limit (Fig. 11) for the sensor.
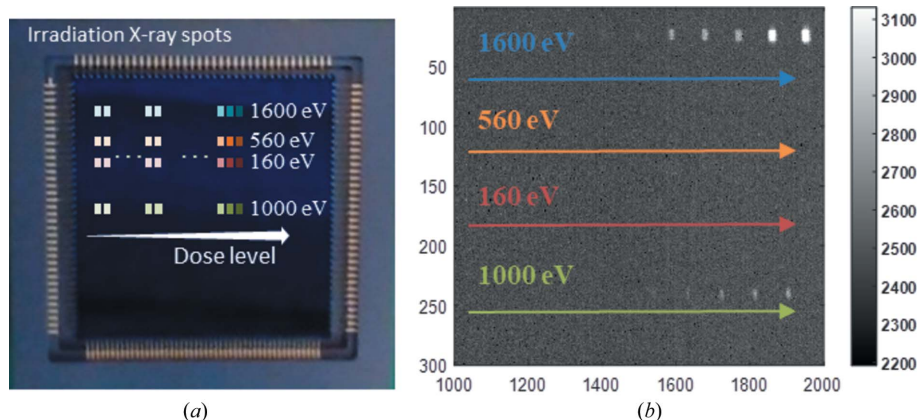

Figure 9
(a) Schematic representation of X-ray irradiation of GSENSE400BSI for 160, 560, 1000 and 1600 eV. (b) Part of GSENSE400BSI-TVISB dark image (300 × 1000 pixels) after irradiation (contrast manually increased).
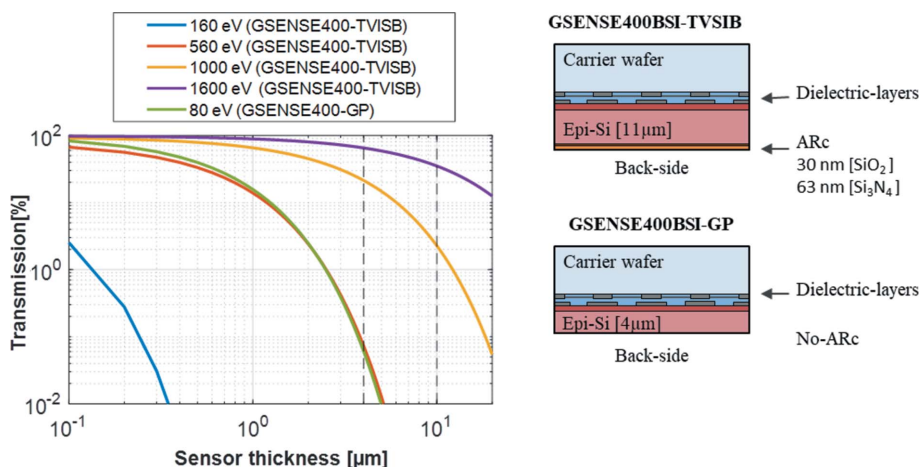

Figure 10
Theoretical transmission versus Si thickness for X-ray photons of 160, 560, 1000 and 1600 eV through the GSENSEBSI400-TVISB and of 80 eV through the GSENSEBSI400-GP. Computed with Matlab toolbox on X-ray *Refraction of Matter* (Jiang, 2020).

The dark level increase, due to the dose, could be fitted (Bogaerts *et al.*, 2003) with an empirical formula such as

$$\text{Idark}_{\text{after irradiation}} - \text{Idark}_0 = \begin{cases} 0, & D < D_{\text{th}}, \\ K \log_{10}\left(\frac{D}{D_{\text{th}}}\right), & D \geq D_{\text{th}}, \end{cases} \quad (5)$$

where D is the dose on the electronic layer [equation (4)], D_{th} is the dose threshold and K a proportionality factor given the offset pixel evolution per (ADU decade^{-1}).

The fitted curve, in Fig. 11(a), for the two high-energy measurements showed a transition at around D_{th} = 600 Gy(SiO$_2$) (60 krad) and K = 125 ADU decade^{-1}. This dose threshold seems to be confirmed by the series of measurements performed on the thinner GSENSE400BSI-GP but with a higher dark evolution proportionality factor of around 4000 ADU decade^{-1} [in Fig. 11(b)].

If the dose limit seems not very high, it should be noted that it is very difficult to compare with other similar devices as this measurement is not easy to perform or easy to exploit and is rarely published. Nonetheless, e2v reports a radiation tolerance of 10 krad (100 Gy) on the classical CCD design (CCD40-42, https://www.e2v.com). Finally, we give in Fig. 12 two examples of the experimental irradiation limitation to avoid damage using the two sensors tested here. In Fig. 12(a), the number of photons per second over 1 pixel to reach D_{th} = 600 Gy(SiO$_2$) is reported. In Fig. 12(b), we considered an incident flux of 10^{10} photons s^{-1} pixel^{-1} which corresponds to 2 decades below the direct beam of the SEXTANTS beamline and the limit of irradiation time to reach D_{th} = 600 Gy(SiO$_2$) is reported.

4. Experiments performed on soft X-ray beamlines using the sCMOS GSENSE400BSI

4.1. Soft X-ray resonant magnetic scattering

The GSENSE400BSI camera has been installed on the RESOXS end-station (Jaouen *et al.*, 2004) of the SEXTANTS beamline at SOLEIL to illustrate its capabilities in the soft X-ray range with an X-ray resonant magnetic scattering (XRMS) experiment (Chauleau *et al.*, 2018). As mentioned above, high resolution, low noise and high charge collection capacity are strongly required for this type of acquisition and have been previously achieved using direct CCD detection. User experiments performed at the beamline routinely employ back-illuminated CCDs of the PIMTE camera from Princeton Instruments (4 Mpixels e2V CCD 42-40, pixel size 13.5 µm, QE > 90% at 700 eV, FWC = 100 ke$^-$, electronic noise of 10 e$^-$ r.m.s. with 0.22 Hz). In order to experimentally compare the performance of the sCMOS camera with this CCD camera, we collected a soft X-ray scattering pattern from an assembly of rectangular dots lithographically carved in a Co/Cu multilayer sample (top left in Fig. 13).
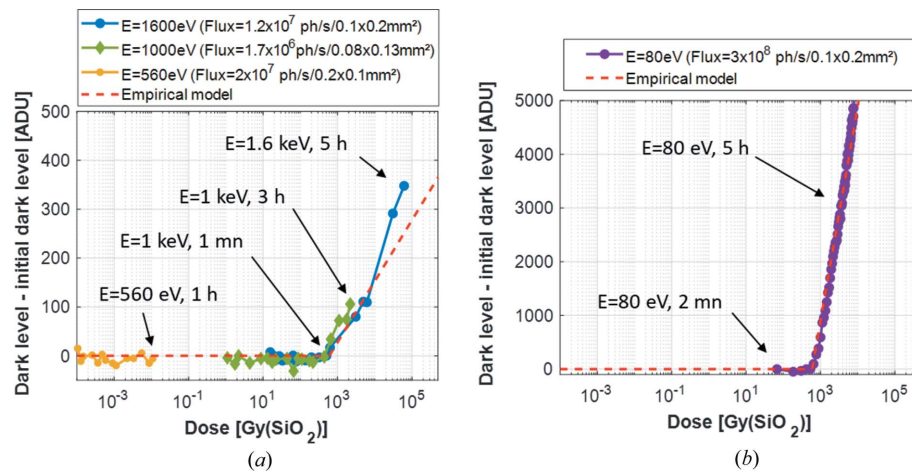
With its present housing (Fig. 3), the sCMOS camera could not be placed inside the ultra-high vacuum (UHV) vessel of the RESOXS scattering chamber, as is the case for the CCD. This implies a large difference in the sample–detector distance, which is 25 cm for the CCD and 1 m for the sCMOS, and, consequently, in the accepted angular aperture (1.5° and 6.3°, respectively). Despite the lack of optimal conditions, similar acquisitions could be performed using the two detectors. Fig. 14 compares two scattering images obtained at 767 eV (Co L3-edge resonance) using the following

Figure 11
Radiation tolerance evaluation of (a) sCMOS GSENSE400BSI-TVISB and (b) sCMOS GENSE400BSI-GP by excess dark measurement after soft X-ray irradiation with a beam of 560, 1000 and 1600 eV and 80 eV, respectively. The dashed red curves are the empirical models [equation (5)].
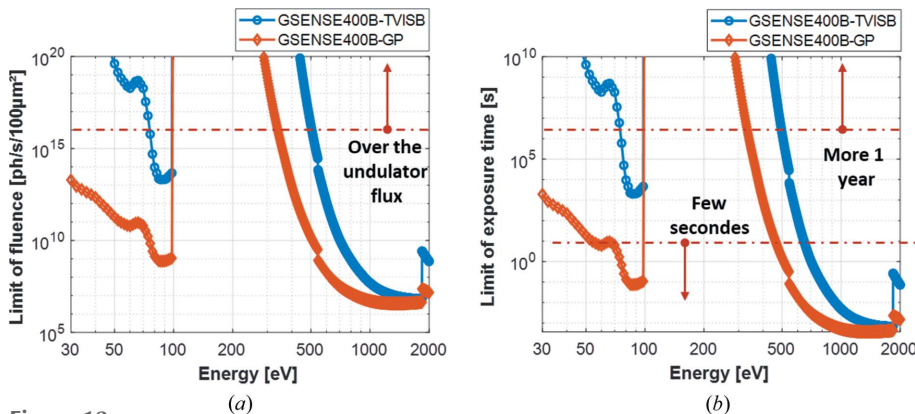

Figure 12
Limit of (a) the flux over 100 µm^2 and (b) the irradiation time considering 10^{10} photons s^{-1} pixel^{-1} calculated for a dose limit of 600 Gy(SiO$_2$) on dielectric layer of GSENSE400BSI-TVISB (blue) and GSENSE400BSI-GP (red) before damage is sustained.
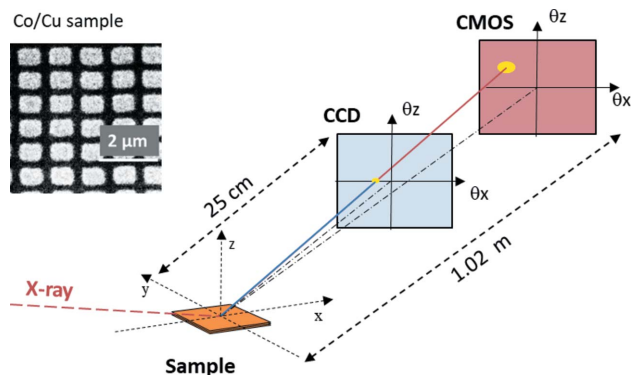
Figure 13
SEXTANTS beamline synoptic for the GSENSE400BSI versus CCD test. In the top left, a scanning electron microscopy (SEM) image of the Co/Cu nanostructured sample used for the test.

parameters: accumulation of 100 images with 200 ms exposure time, setting the HDR mode for the GSENSE400BSI sensor and the analog-to-digital converter (ADC) 1 MHz mode for the CCD. In addition to the raw images (in pixels), Fig. 15 compares the results on a common angular scale, measuring the position of the scattered beam with respect to the specular one.

The beam was focused at the CCD position and its divergence is a few mrad, which explains why the diffracted spots are wider in the sCMOS image. To compare these images, the
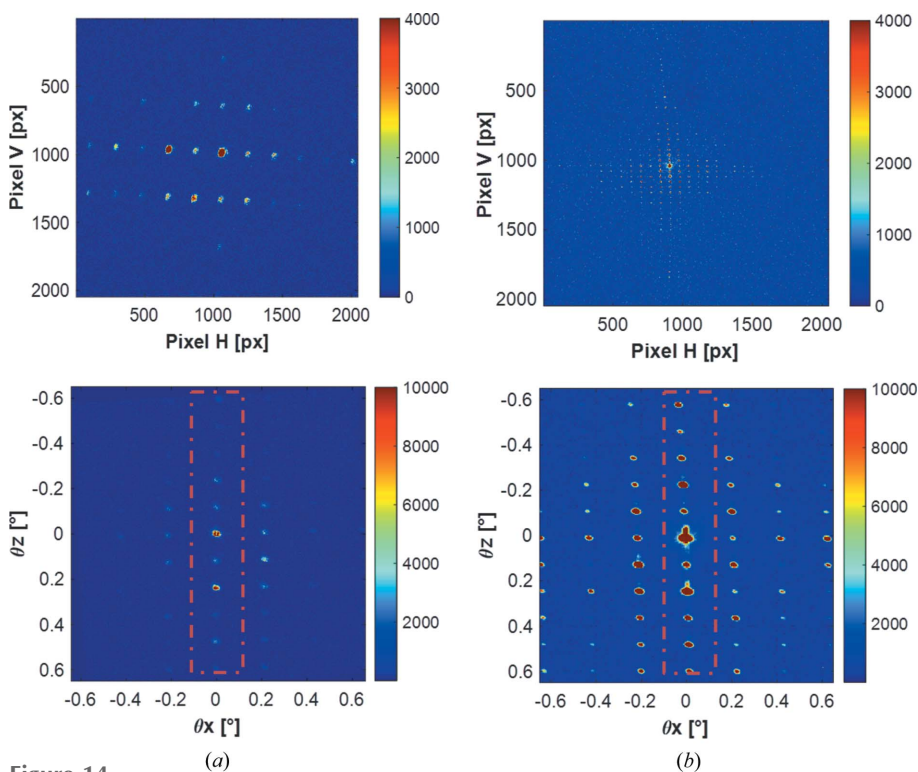
spatial coordinates defined by the detector pixels (top images of Fig. 14) are transposed into angular coordinates of the scattered photons, measured with respect to the specular reflection, within (θx) and orthogonal to (θz) the incidence plane.

Line profiles drawn along the θz direction are compared in Fig. 15 for the two acquisitions. They show similar intensity distributions with a nice superposition of the diffraction peaks originating from the regular pattern of the sample (top left in Fig. 13). Slightly different modulations of the scattered intensity can be observed, particularly close to the specular reflection.

As the beam focusing, aperture, pixel size and QE are not the same, the magnitudes of the scattered intensity are not easy to compare directly. A new series of dedicated experiments is planned to obtain a more quantitative comparison of efficiency and SNR performance between our in-vacuum sCMOS detector and the well known and widely employed CCD BSI. At this stage, we can conclude that images of similar quality have been obtained integrating 100 frames of 200 ms acquisition time using either the sCMOS or the CCD detector. It should be stressed, however, that the total measuring time is quite different in the two cases, being merely 20 s for the sCMOS (100 frames times 0.2 s) against some 7 min for the CCD, due to its 4 s frame^{-1} readout time. The corresponding duty cycles are 100% for the sCMOS and 5% for the CCD.

This optimization of the duty cycle may change drastically; for instance, the measuring time in a Fourier transform holography imaging experiment, bringing it from typically 1 h today to a few minutes in the near future.

This represents an important gain for imaging experiments in which we have to scan an external parameter (magnetic field, electric field, temperature), and is even more important for time-resolved experiments (Bukin *et al.*, 2016). The capability to acquire images with a much higher frame rate will also dramatically expand the time window available at SEXTANTS for resonant magnetic soft X-ray photon correlation spectroscopy (XPCS), examples of which have been obtained only recently at NSLS2 using a fast CCD (Chen *et al.*, 2019). Lastly, it will also be a real gain for soft X-ray resonant ptychography in reflection geometry that is nowadays limited only by the coherent flux available and by mechanical instabilities (Popescu *et al.*, 2019). It is important also to note that all these improvements will become even more important at the new storage rings presently under development: the expected huge
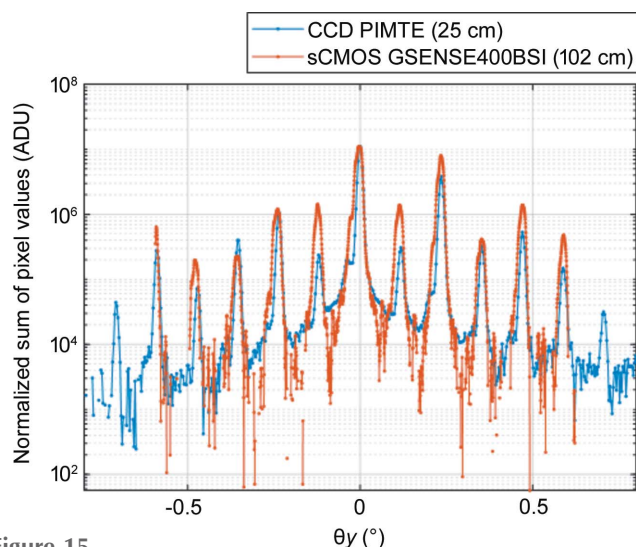

Figure 14
Dark-corrected images of soft X-ray scattering from an array of Co/Cu multilayered dots acquired using 767 eV with (*a*) the sCMOS GSENSE400BSI camera placed at 1 m from the sample and (*b*) the PIMTE camera placed at 25 cm from the sample. The images correspond to the accumulation of 100 frames, each one integrated for 200 ms. Top: raw images from the two detectors. Bottom: same data reframed on a common angular scale, $\theta x,y$ being measured with respect to the specular beam.

Kewin Desjardins *et al.* · Backside-illuminated scientific CMOS detector   **1585**

Figure 15
Superposition of the sum of the pixels normalized in the central region of the images (Fig. 14) obtained with the CCD camera (blue line) and the sCMOS camera (red line) for a photon energy of 767 eV versus the orthogonal angle.

increase in coherent flux, for instance, will further decrease the typical exposure time per frame, rendering the reduction of the detector readout time an ever more important parameter.

4.2. Soft X-ray ptychography reconstruction

At the HERMES beamline, a soft X-ray beamline dedicated to X-ray microscopy and equipped for scanning transmission X-ray microscopy (STXM) at SOLEIL, a new dedicated setup for soft X-ray ptychography has recently been implemented to improve the spatial resolution capability of the beamline by replacing the 1D detector (scintillator photomultiplier tube, PMT) with the sCMOS GSENSE400BSI camera. Ptychography is the combination of diffraction imaging and scanning transmission microscopy which provides images of extended sample areas utilizing iterative reconstruction algorithms, giving phase and amplitude information

for the studied specimens. It is able to reach ultimate spatial resolutions well below 10 nm, while in contrast the resolution in standard X-ray microscopes is limited by the focusing element, e.g. Fresnel zone plates (FZP), and stays in the range of 20 nm for highly efficient zone plates. Diffraction imaging techniques with the use of coherent X-ray radiation can potentially achieve wavelength-limited resolution by solving the so-called 'phase problem'. This new setup effectively replaces the measurement of transmitted intensity through a sample scanned in 2D by measurement of the transmitted diffraction patterns recorded by the sCMOS camera.

In order to illustrate the capability of this new setup, test experiments were performed in ptychography mode on a 200 nm-thick Au Siemens star pattern at 706 eV. Typically, diffraction patterns were collected in raster mode, by scanning a 1 µm^2 sample area with a step size of 15 or 20 nm, ensuring an oversampling better than 50%. Thanks to the fast readout of the camera and its sensitivity, the dwell time per point could be varied from 50 to 500 ms, keeping the experiment time to a reasonable amount. Compared with a standard ptychography approach using a parallel beam, the advantage in this case is the possibility to rapidly extract the STXM image by integrating the overall intensity on the camera, as shown in Fig. 16(a).

The image presented in Fig. 16(a) is the initial image obtained by integrating the images of each step; that in Fig. 16(b) is the resulting image from the ptychographic reconstruction obtained from the recorded diffraction patterns, such as the typical one shown in Fig. 16(c), using the extended ptychography iterative engine method recently implemented in the upgraded Matlab version of MMX-I (Medjoubi et al., 2018) developed by the NANOSCOPIUM beamline and used by several SOLEIL beamlines.

Further demonstration of the setup performances is given by the measurements performed on magnetotactic bacteria (magnetosomes). The images were obtained at 706 eV, with a step size of 15 nm, ensuring an adjacent spot overlap of 70%. A region of interest (1024 × 1024 pixels) was selected on the sCMOS which allows the frame rate to be increased to 44 Hz
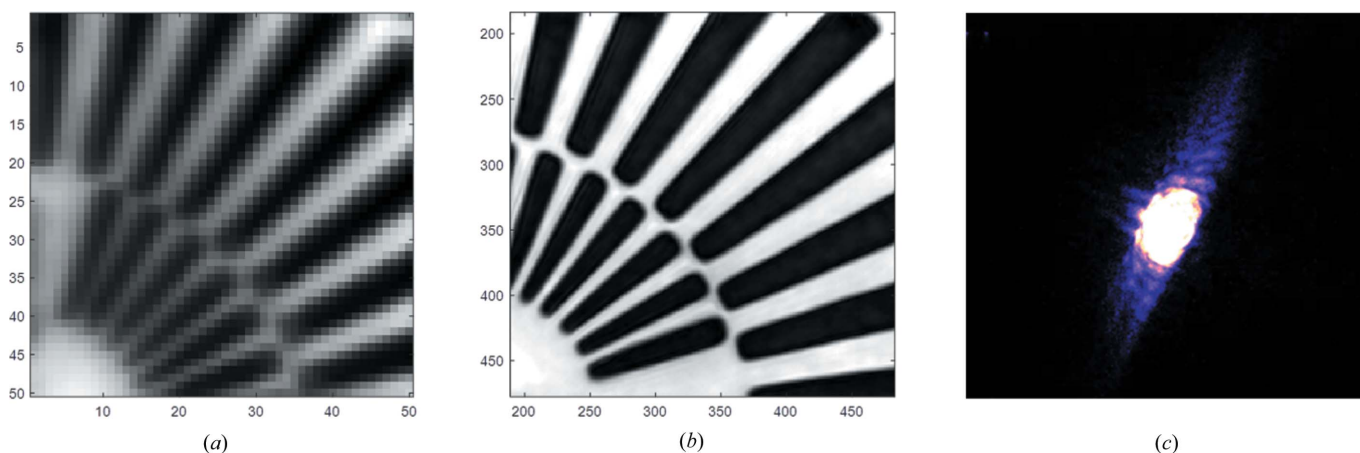

Figure 16
(a) STXM image with a beam of 61 nm and a step size of 15 nm. (b) Ptychography reconstruction of the Siemens star. (c) Diffraction pattern image of a part of the Siemens star.
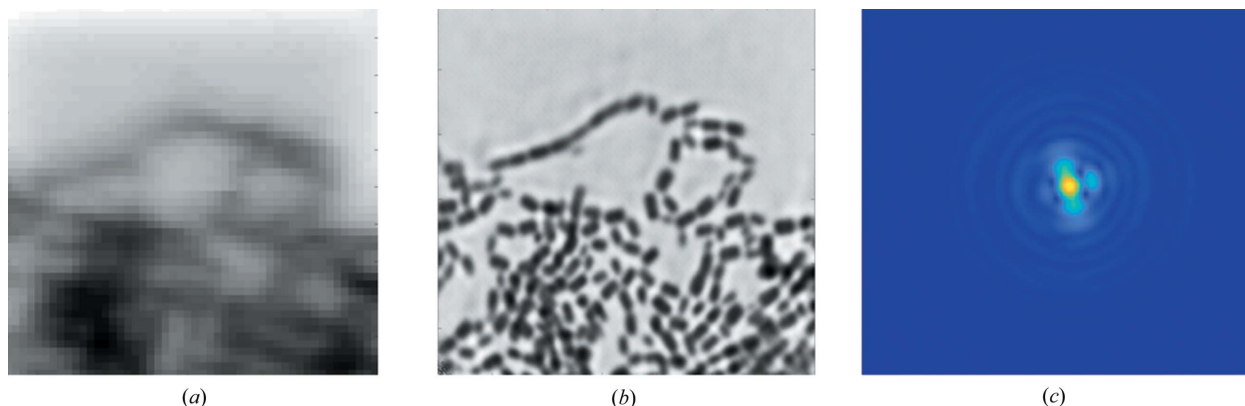
Figure 17
(*a*) Integrated intensity STXM image of magnetosomes at 706 eV. (*b*) Ptychography reconstruction of the magnetosome. (*c*) Image of the reconstructed amplitude of the X-ray probe.

(HDR mode) thus reducing the total acquisition time to 10 min. Fig. 17(*a*) shows the low-resolution classical STXM image obtained by image integration, Fig. 17(*b*) shows the reconstructed ptychography image from a speckle pattern image, and Fig. 17(*c*) is an example of an amplitude measurement. This reconstruction allows bacterial magnetosomes with an average size of <25 nm to be clearly observed, well beyond the resolution of the zone plates used (outer ring width 50 nm). The strong absorption contrast at 706 eV allows the observation of intercellular space between two adjacent magnetosomes (5 to 10 nm).

The potential of the ptychography setup using the sCMOS camera is evident from the two examples cited above. A gain in spatial resolution, not limited by the zone plate, would eventually allow a host of new experiments. Compared with a CCD, the intrinsic advantages include: fast readout, ease of use since there is no need for complex setups involving additional shutters, price *etc.* During the experiments the camera was installed on the STXM detector stage allowing the experimental geometry to be optimized easily and quickly, *i.e.* sample-to-camera distance, to the energy range, thus optimizing the diffracted pattern with respect to the chipset and pixel size. The proof-of-principle experiments shown above were performed at an energy chosen to provide a good QE (700 eV) with respect to the sensor. Future developments aim at using the high-frame-rate capabilities of the sCMOS in conjunction with a newly developed coating-free chipset that will allow ptychography experiments at the C *K* edge. In the framework of the upcoming SOLEIL's upgrade, the spectro-microscopy in ptychography approach at the STXM instrument would provide a new standard working mode, benefiting from the higher coherence and brilliance of the new source.

5. Summary and perspectives

A new camera based on the first commercially available backside-illuminated scientific CMOS sensor GSENSE400BSI was developed and evaluated for soft X-ray applications on several beamlines at the SOLEIL synchrotron. This solution, which requires neither a new microelectronics design nor a large collaboration, can be adapted to particular applications

at a very attractive cost. The QE is suited to a large field of application in the soft X-ray domain (QE > 50% for $E >$ 400 eV) and the new no-ARc sensor has already demonstrated a high QE of >90% in the lower-energy range and more importantly across the water window region. The readout noise (<2 e^- r.m.s.) and the FWC provide a good X-ray dynamic range and an interesting single-photon detection capability without any decrease of the readout speed performance. This sensor has a frame rate up to 48 Hz (in standard mode) which allows the acquisition time for imaging applications to be dramatically reduced compared with the classical cameras commonly used. The new optimized version of the acquisition board allows the performance to be further improved with a lower spatial noise with DSNU < 0.2 e^-, a PRNU of 0.3% and a FWC of 80 ke$^-$ (in HDR mode). The soft X-ray spatial and energy resolution has been confirmed with a limitation for lower energies due to the dead layer thickness and the thick Epi-Si layers. As for similar synchrotron direct X-ray detectors, the radiation hardness is a significant challenge in order to maintain good performances with a high density of flux. The dose limit of 600 Gy(SiO$_2$) has been measured that will allow researchers to adapt the experimental conditions and setup in order to avoid damage to the sensor. A compact, cooled vacuum-compatible camera prototype has been developed, which can easily be installed in the experimental end-stations of the SEXTANTS and HERMES beamlines at SOLEIL. A first soft X-ray resonant scattering (REXS) acquisition from a nanostructured multilayer sample has been performed on the SEXTANTS beamline, showing a good dynamic range with a factor of 24 reduction in acquisition time compared with the usual detector. A fully functional soft X-ray ptychography setup based on this sCMOS camera has been used on the STXM end-station at the HERMES beamline. Its performances and frame rate have been demonstrated by several reconstructions showing good spatial resolution.

Lastly, a new GSENSE400BSI sensor version with a thicker Epi-Si and a highly efficient process has been tested by Harada at the NewSUBARU synchrotron facility (Harada *et al.*, 2020). It assures a very good efficiency (>80%) over a very large soft X-ray range and it will soon be commercially

available from GPIXEL. This new sensor will be used in the second sCMOS camera for HERMES to increase performance, particularly for experiments at the so-called water window's carbon *K* edge. Also, the other camera will soon be installed in the SEXTANTS COMET end-station in order to optimize the acquisition time for magnetic imaging using Fourier transform holography.

Based on these first results and the enthusiasm of the scientific community for this cost-efficient solution, a Canadian company specialized in high-speed camera solutions, Axis Photonique (https://www.axis-photon.com), is now proposing a new soft X-ray sCMOS detector based on the SOLEIL prototype. Furthermore, other potential domains could be explored: another synchrotron beamline application, such as tender X-ray SAXS (>1.2 keV) at the SIRIUS beamline at SOLEIL, or for lower soft X-ray photon sources based on femtosecond lasers or for soft XFELs. In particular, a test of our camera has already been planned in the next few months at FERMI.

To conclude, the first back-illuminated sCMOS implementation reported in this paper could be considered as the beginning of a long series of new detectors based on this technology.

References

Arai, Y., Miyoshi, T., Unno, Y., Tsuboyama, T., Terada, S., Ikegami, Y., Kohriki, T., Tauchi, K., Ikemoto, Y., Ichimiya, R., Ikeda, H., Hara, K., Miyake, H., Kochiyama, M., Sega, T., Hanagaki, K., Hirose, M., Hatsui, T., Kudo, T., Hirono, T., Yabashi, M., Furukawa, Y., Varner, G., Cooney, M., Hoedlmoser, H., Kennedy, J., Sahoo, H., Battaglia, M., Denes, P., Vu, C., Contarato, D., Giubilato, P., Glesener, L., Yarema, R., Lipton, R., Deptuch, G., Trimpl, M., Ohno, M., Fukuda, K., Komatsubara, H., Ida, J., Okihara, M., Hayashi, H., Kawai, Y. & Ohtomo, A. (2010). *Nucl. Instrum. Methods Phys. Res. A*, **623**, 186–188.

Belkhou, R., Stanescu, S., Swaraj, S., Besson, A., Ledoux, M., Hajlaoui, M. & Dalle, D. (2015). *J. Synchrotron Rad.* **22**, 968–979.

Bergamaschi, A., Andrä, M., Barten, R., Borca, C., Brückner, M., Chiriotti, S., Dinapoli, R., Fröjdh, E., Greiffenberg, D., Huthwelker, T., Kleibert, A., Langer, M., Lebugle, M., Lopez-Cuenca, C., Mezza, D., Mozzanica, A., Raabe, J., Redford, S., Ruder, C., Scagnoli, V., Schmitt, B., Shi, X., Staub, U., Thattil, D., Tinti, G., Vaz, C. F., Vetter, S., Vila-Comamala, J. & Zhang, J. (2018). *Synchrotron Radiat. News*, **31**, 11–15.

Bogaerts, J., Dierickx, B., Meynants, G. & Uwaerts, D. (2003). *IEEE Trans. Electron Devices*, **50**, 84–90.

Bukin, N., McKeever, C., Burgos-Parra, E., Keatley, P. S., Hicken, R. J., Ogrin, F. Y., Beutier, G., Dupraz, M., Popescu, H., Jaouen, N.,

Yakhou-Harris, F., Cavill, S. A. & van der Laan, G. (2016). *Sci Rep*, **6**, 36307.

Burns, P. (2009). *SFRmat3 script* (http://losburns.com). Matlab script.

Chauleau, J. Y., Legrand, W., Reyren, N., Maccariello, D., Collin, S., Popescu, H., Bouzehouane, K., Cros, V., Jaouen, N. & Fert, A. (2018). *Phys. Rev. Lett.* **120**, 037202.

Chen, X., Farmer, B., Woods, J., Dhuey, S., Hu, W., Mazzoli, C., Wilkins, S., Chopdekar, R., Scholl, A., Robinson, I., De Long, L., Roy, S. & Hastings, J. (2019). *Phys. Rev. Lett.* **123**, 197202..

Clarke, R. (1994). *Nucl. Instrum. Methods Phys. Res. A*, **347**, 529–533.

Deiries, S., Lizon, J. L. & Iwert, O. (2016). *Proc. SPIE*, **9912**, 99125Y.

Denes, P., Doering, D., Padmore, H. A., Walder, J. P. & Weizeorick, J. (2009). *Rev. Sci. Instrum.* **80**, 083302.

Desjardins, K., Popescu, H., Mercère, P., Menneglier, C., Gaudemer, R., Thånell, K. & Jaouen, N. (2019). *AIP Conf. Proc.* **2054**, 060066.

El Bitar, Z., Heymes, J., Kachel, M., Baudot, J., Hu-Guo, C. & Winter, M. (2019). *International Conference on Advances in Biomedical Engineering (ICABME)*, Vol. 2019, October, pp. 1–4. IEEE.

Förster, A., Brandstetter, S. & Schulze-Briese, C. (2019). *Philos. Trans. R. Soc. A.* **377**, 20180241.

Hancock, B. R. & Soli, G. A. (1997). *IEEE Trans. Nucl. Sci.* **44**, 1957–1964.

Harada, T., Teranishi, N., Watanabe, T., Zhou, Q., Bogaerts, J. & Wang, X. (2020). *Appl. Phys. Express*, **13**, 016502.

Harada, T., Teranishi, N., Watanabe, T., Zhou, Q., Yang, X., Bogaerts, J. & Wang, X. (2019). *Appl. Phys. Express*, **12**, 082012.

Idir, M., Mercere, P., Moreno, T. & Delmotte, A. (2006). *Synchrotron Radiat. News*, **19**, 18–23.

ISO (2000). ISO 12233:2000(E). International Organization for Standardization, Geneva, Switzerland.

Janesick, J. R. (2001). *Scientific Charge-Coupled Devices*. Bellingham: SPIE Press.

Jaouen, N., Tonnerre, J.-M., Kapoujian, G., Taunier, P., Roux, J.-P., Raoux, D. & Sirotti, F. (2004). *J. Synchrotron Rad.* **11**, 353–357.

Jiang, Z. (2020). *Toolbox: X-ray Refraction of Matter* (https://www.mathworks.com/matlabcentral/fileexchange/6026-toolbox-x-ray-refraction-of-matter). Matlab Central File Exchange.

Jungmann-Smith, J. H., Bergamaschi, A., Brückner, M., Cartier, S., Dinapoli, R., Greiffenberg, D., Huthwelker, T., Maliakal, D., Mayilyan, D., Medjoubi, K., Mezza, D., Mozzanica, A., Ramilli, M., Ruder, C., Schädler, L., Schmitt, B., Shi, X. & Tinti, G. (2016). *J. Synchrotron Rad.* **23**, 385–394.

Khromova, A., Cautero, G., Giuressi, D., Menk, R., Pinaroli, G., Stebel, L., Correa, J., Marras, A., Wunderer, C. B., Lange, S., Tennert, M., Niemann, M., Hirsemann, H., Smoljanin, S., Reza, S., Graafsma, H., Göttlicher, P., Shevyakov, I., Supra, J., Xia, Q., Zimmer, M., Guerrini, N., Marsh, B., Sedgwick, I., Nicholls, T., Turchetta, R., Pedersen, U., Tartoni, N., Hyun, H. J., Kim, K. S., Rah, S. Y., Hoenk, M. E., Jewell, A. D., Jones, T. J. & Nikzad, S. (2016). *J. Instrum.* **11**, C11020.

Lambert, G., Vodungbo, B., Gautier, J., Mahieu, B., Malka, V., Sebban, S., Zeitoun, P., Luning, J., Perron, J., Andreev, A., Stremoukhov, S., Ardana-Lamas, F., Dax, A., Hauri, C. P., Sardinha, A. & Fajardo, M. (2015). *Nat. Commun.* **6**, 6–11.

Lumb, D. H., Hopkinson, G. R. & Wells, A. A. (1984). *Nucl. Instrum. Methods Phys. Res.* **221**, 150–158.

Ma, C., Liu, Y., Li, J., Zhou, Q., Chang, Y. & Wang, X. (2015). *Proc. SPIE*, **9403**, 940305.

Medjoubi, K., Baranton, G. & Somogyi, A. (2018). *Microsc. Microanal.* **24**, 252–253.

Pedersoli, E., Capotondi, F., Cocco, D., Zangrando, M., Kaulich, B., Menk, R. H., Locatelli, A., Mentes, T. O., Spezzani, C., Sandrin, G., Bacescu, D. M., Kiskinova, M., Bajt, S., Barthelmess, M., Barty, A., Schulz, J., Gumprecht, L., Chapman, H. N., Nelson, A. J., Frank, M., Pivovaroff, M. J., Woods, B. W., Bogan, M. J. & Hajdu, J. (2011). *Rev. Sci. Instrum.* **82**, 043711.

Popescu, H., Perron, J., Pilette, B., Vacheresse, R., Pinty, V., Gaudemer, R., Sacchi, M., Delaunay, R., Fortuna, F., Medjoubi,

K., Desjardins, K., Luning, J. & Jaouen, N. (2019). *J. Synchrotron Rad.* **26**, 280–290.

Porro, M., Andricek, L., Aschauer, S., Bayer, M., Becker, J., Bombelli, L., Castoldi, A., De Vita, G., Diehl, I., Erdinger, F., Facchinetti, S., Fiorini, C., Fischer, P., Gerlach, T., Graafsma, H., Guazzoni, C., Hansen, K., Kalavakuru, P., Klär, H., Kugel, A., Lechner, P., Lemke, M., Lutz, G., Manghisoni, M., Mezza, D., Müntefering, D., Pietsch, U., Quartieri, E., Randall, M., Re, V., Reckleben, C., Sandow, C., Soldat, J., Strüder, L., Szymanski, J., Weidenspointner, G. & Wunderer, C. B. (2012). *IEEE Trans. Nucl. Sci.* **59**, 3339–3351.

Ravotti, F. (2018). *IEEE Trans. Nucl. Sci.* **65**, 1440–1464.

Sacchi, M., Jaouen, N., Popescu, H., Gaudemer, R., Tonnerre, J. M., Chiuzbaian, S. G., Hague, C. F., Delmotte, A., Dubuisson, J. M., Cauchon, G., Lagarde, B. & Polack, F. (2013). *J. Phys. Conf. Ser.* **425**, 0–4.

Spear, J. D. (2005). *Rev. Sci. Instrum.* **76**, 076101.

Strüder, L. (2016). In *Synchrotron Light Sources and Free-Electron Lasers*, edited by E. J. Jaeschke, S. Khan, J. R. Schneider & J. B. Hastings. Cham: Springer.

Wang, W. X., Ling, Z. X., Zhang, C., Jia, Z. Q., Wang, X. Y., Wu, Q., Yuan, W. M. & Zhang, S. N. (2019). *J. Instrum.* **14**, P02025.

Wang, Y., Zhao, L., Hu, Z., Wang, Y., Zhao, Z., Li, L. & Huang, Z. L. (2017). *Cytometry*, **91**, 1175–1183.

Wunderer, C. B., Marras, A., Bayer, M., Glaser, L., Göttlicher, P., Lange, S., Pithan, F., Scholz, F., Seltmann, J., Shevyakov, I., Smoljanin, S., Viefhaus, J., Viti, M., Xia, Q., Zimmer, M., Klumpp, S., Gasiorek, P., Guerrini, N., Marsh, B., Sedgwick, I., Turchetta, R., Cautero, G., Farina, S., Giuressi, D., Menk, R., Stebel, L., Yousef, H., Marchal, J., Nicholls, T., Tartoni, N. & Graafsma, H. (2014). *J. Instrum.* **9**, C03056.